

# Assessment of mitigation strategies for tropospheric phase contributions to InSAR time-series datasets over two Nicaraguan volcanoes

Kirsten J. Stephens, Christelle Wauthier, Rebecca Bussard and Machel Higgins & Peter C. LaFemina

## Supplementary Material:

### Computation of semivariogram structure functions to examine atmospheric noise

Semivariograms are spatial structure functions that are useful for examining the variability within InSAR deformation fields as a function of distance between selected data point pairs [1–5]. The classical variogram estimator ( $\gamma(H)$ ) is computed as follows [6–8]:

$$\gamma(H) = \frac{1}{2|N(H)|} \cdot \sum_{i=1}^{|N(H)|} (z_i - z_{i+H})^2 \quad (6)$$

Where  $H$  is the lag interval,  $|N(H)|$  is the number of pairs within the lag interval, and  $z_i$  and  $z_{i+H}$  are the values at the data point located at point  $i$  and  $i+H$ , respectively. The point at which the experimental variogram does not continue to increase with increasing semivariance is known as the “sill”, and the distance at which this occurs is known as the “range”. The “sill” indicates the lag distance at which two points of interest are dissimilar from each other [9]. The “nugget-effect” is observed when the variogram is not differentiable at zero lag distance, and indicates that the variance within the image being analysed changes abruptly at distances smaller than that of the sample spacing [9,10]. While atmospheric noise in interferograms can have directional dependence [1–3], we assume that the noise in the non-deforming and neighboring deforming regions within the Telica and Masaya scenes is the same, and focus only on the impact of the length of the lag interval (distance) [5,10]. Following the recommendation of Bagnardi & Hooper [10], we performed our semivariogram analyses over the entire CSK scene and masked out regions of potential deformation specific to each case study region. The square-root of the semivariance was computed for comparison with the semivariograms given in Murray et al. [5]. We examined the semivariogram plots for each individual interferogram, and also averaged all semivariograms within each InSAR uncorrected and corrected dataset to examine the correlation of atmospheric noise with distance between the different corrected InSAR datasets as a whole.

The majority of InSAR studies that examine the applicability of GWMs typically involve SAR data spanning >50 km [5,11–15]. Volcanic regions, however, can span anywhere between 2 km to 40 km spatially [16], and thus the spatial resolution of the GWMs limits the ability to remove potential atmospheric artifacts on these scales. Examination of semivariogram results for each uncorrected and corrected interferogram for both Telica and Masaya case study regions demonstrate that the structure of the atmospheric noise varies greatly in terms of magnitude and on spatial scales from interferogram to interferogram (see selected Telica interferogram semivariograms shown in Figure S6). For time-series studies which incorporate hundreds of interferograms, interpreting semivariograms individually becomes tedious and subjective, particularly when the semivariogram does not follow a “typical” pattern (Figure S6, panel d). For example, in a few semivariograms, the linear corrected semivariogram demonstrates a small peak in the semivariance for lag distances less than 10 km (Figure S6, panel a). A similar observation is seen in about 26 GACOS corrected semivariograms for the Telica scenes, where one to two sharp peaks in semivariance are observed

below 18 km lag distance. The GACOS corrected semivariograms shown in Figure S6, panel d, have two peaks around 4 km and 11 km lag distances. After about 18 km lag distance, the semivariance drops to below that of the uncorrected and remaining corrected semivariograms. These peaks are also captured in the averaged semivariograms (Figure S7).

Figure S7 depicts the average semivariance of all uncorrected and corrected interferograms for Telica and Masaya. The general structure of the averaged semivariograms indicate an overall increase in semivariance with an increase in lag distance. In general, the linear correction does not appear to reduce the semivariance greatly, and typically plot just above or below the uncorrected semivariogram. Overall, ERA5 appears to reduce the variance the most at Telica, and GACOS appears to reduce the variance the most at Masaya. A “sill” observed in semivariograms essentially delimits that there is no correlation between pixels that are separated by distances greater than the range [5,9]. For the Masaya semivariograms, we observe a change in slope around 30 km (Figure S7, panel c). This change in gradient is however not observed in the Telica semivariograms (Figure S7, panel a). The increasing semivariance with distance between 0-38 km suggests that large spatial scale signals are present within the Telica interferograms at spatial scales greater than that of the scene, such as orbital errors or large-scale atmospheric effects [5]. Previous estimates suggest that the atmospheric noise can have spatial scales ranging between 5 to 40 km [1,4,17], and our results fall within this range. In general, all of the semivariograms exhibit a nugget semivariance ranging 0.55 to 0.71 cm, which indicates that there are potentially turbulent tropospheric phase delays present within the interferograms at distances smaller than the sample spacing (90 m). From the averaged semivariogram results, we observe that at ~10 km lag distance the average variance ranges between 1.5–1.75 cm for both case study sites. Our results are double that observed in theoretical estimates of atmospheric noise over the Mojave desert in California, in which ~0.8 cm variance was observed at 10 km lag distance [18], confirming that there would indeed be greater difficulty in trying to capture tropospheric phase delays in our case study regions.

**Supplementary Figures**

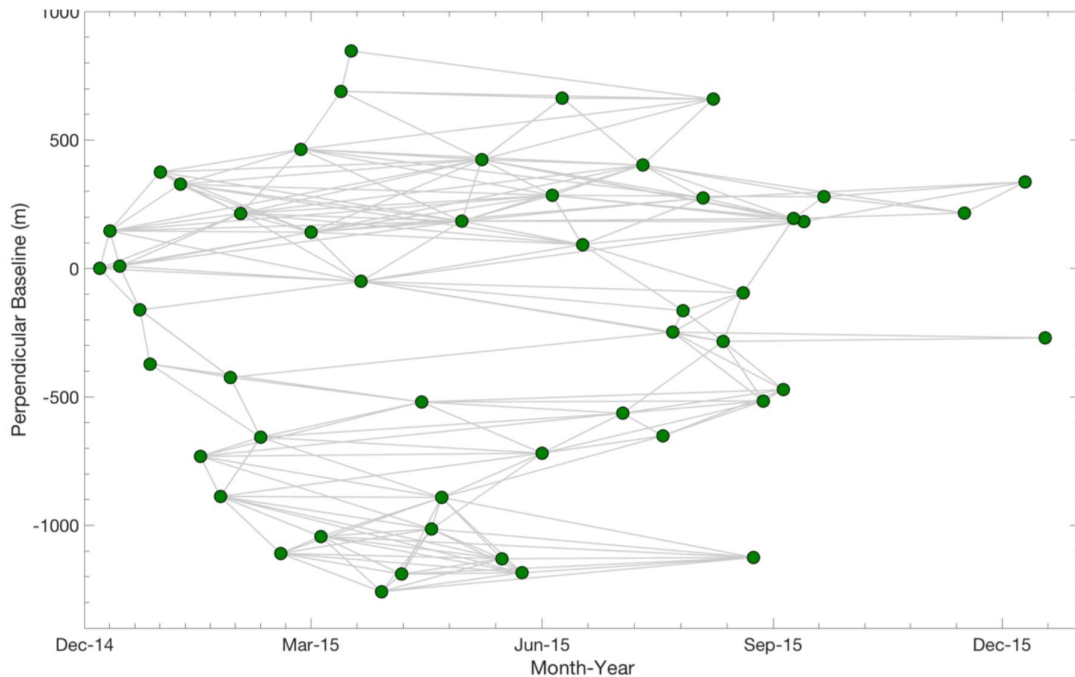


**Figure S1.** Plot of the perpendicular baselines versus Telica CSK acquisition dates. The green dots represent the 50 CSK acquisition dates, with the first date set to zero perpendicular baseline. A

threshold of 300 m or less perpendicular baseline and a temporal threshold of less than 180 days were used to create 199 interferogram pairs (grey lines).

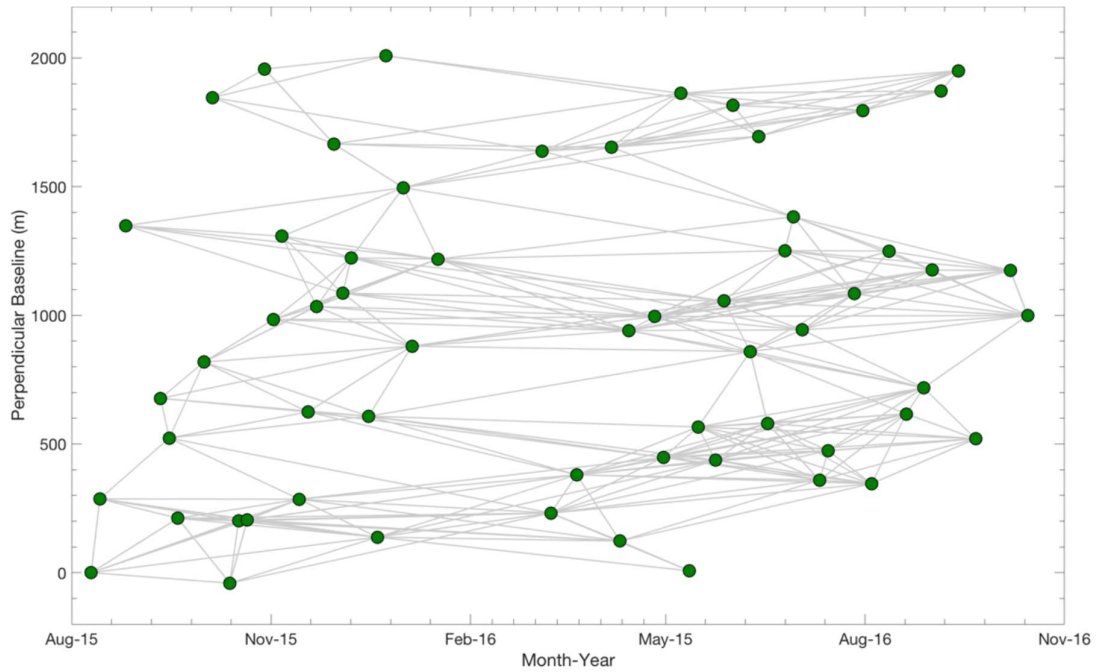


**Figure S2.** Plot of the perpendicular baselines versus Masaya CSK acquisition dates. The green dots represent the 60 CSK acquisition dates, with the first date set to zero perpendicular baseline. A threshold of 300 m or less perpendicular baseline and a temporal threshold of less than 180 days were used to create 281 interferogram pairs (grey lines).

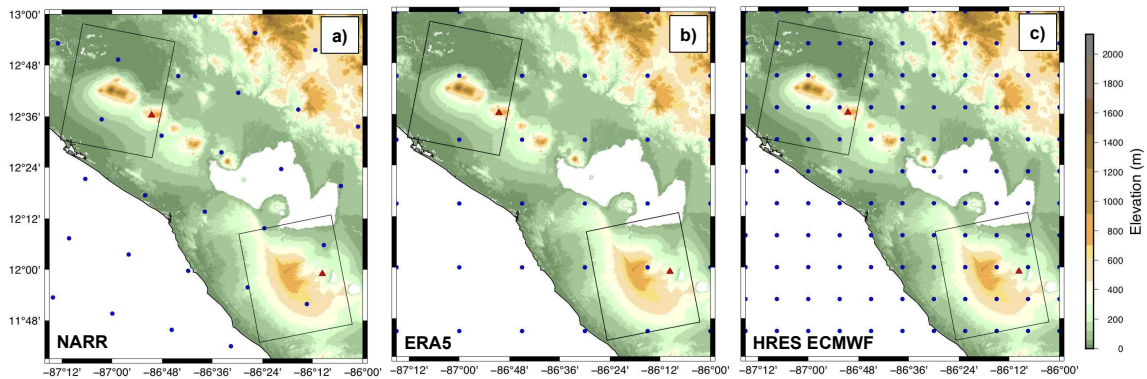


**Figure S3.** Geographic maps displaying the topography of Nicaragua, location of Telica and Masaya volcanoes (red triangles), descending and ascending CSK tracks (black boxes), and the grid nodes for the GWMs (blue circles). a) NARR grid, b) ERA5 grid, and c) HRES CMWF grid. These maps were created using the GMT6 public domain software [19].

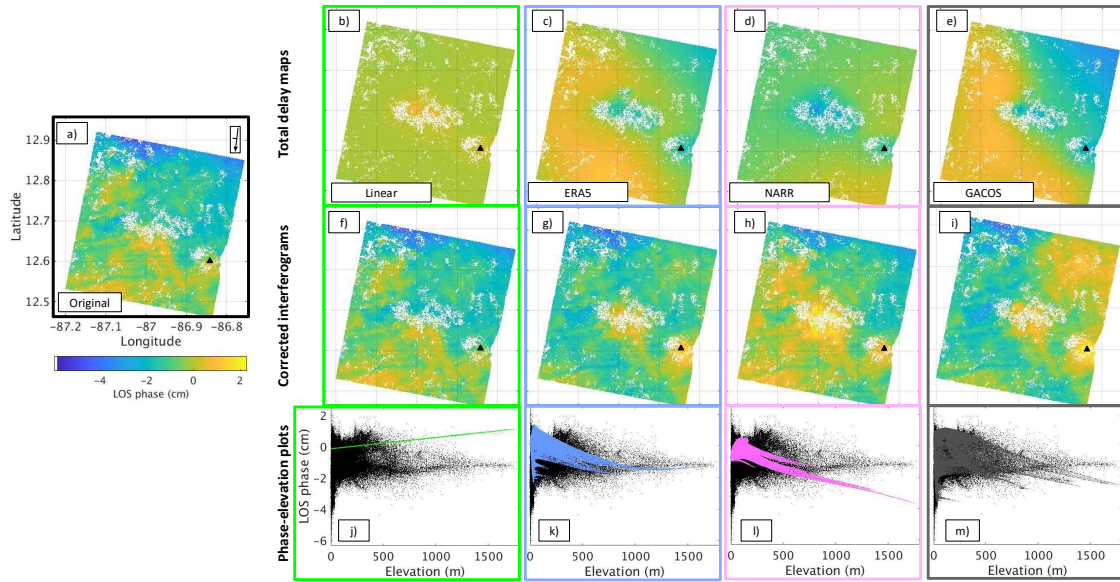


**Figure S4.** Comparison of the different tropospheric phase delay correction methods using Telica unwrapped interferogram 20141223-20141227. a) Uncorrected interferogram, b-e) Total tropospheric delay map for each correction method, f-i) Corrected interferograms using the tropospheric delay maps in the first row, and j-m) Phase-elevation plots of the uncorrected interferogram (black dots) versus the total delay map (colored dots). The geographic extent and colorbar scale for all the interferograms and delay maps are the same, as indicated in panel (a). The colorbar scale for the GACOS data is indicated on the GACOS total delay map. The black triangles in the interferograms and maps indicate the location of Telica volcano in the CSK scene, which is masked out for the phase-elevation plots.

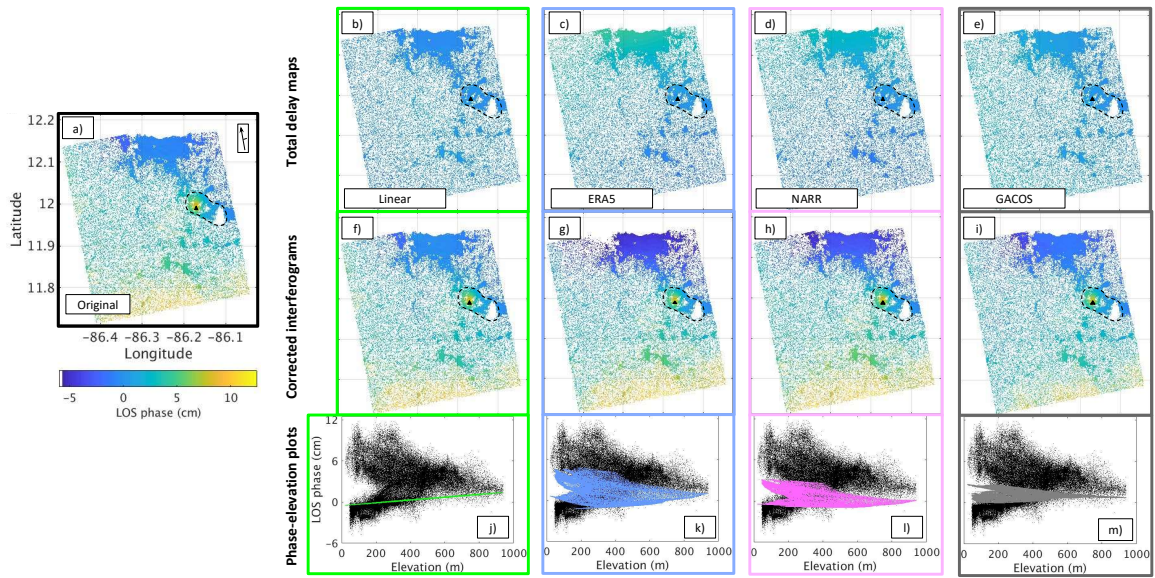


**Figure S5.** Comparison of the different tropospheric phase delay correction methods for Masaya unwrapped interferogram 20151013-20160309. a) Uncorrected interferogram, b-e) Total tropospheric delay map for each correction method, f-i) Corrected interferograms using the tropospheric delay maps from the first row, and j-m) Phase-elevation plots of the uncorrected interferogram (black dots) versus the total delay map (colored dots). The geographic extent and colorbar scale for all the interferograms and delay maps are the same, as indicated for panel (a). The black triangles in the

interferograms and maps indicate the location of the summit of Masaya in the CSK scene, and the dashed outline of the caldera.

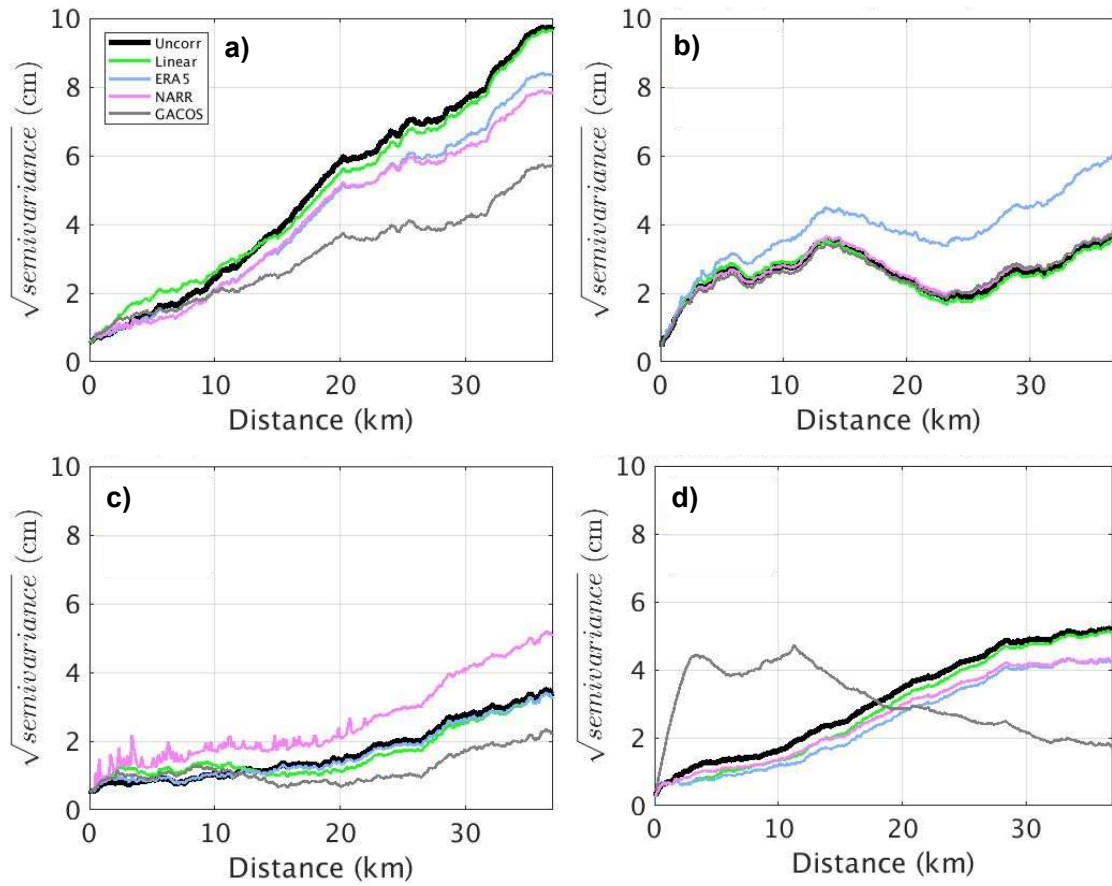


**Figure S6.** Examples of semivariogram plots for selected Telica CSK uncorrected and corrected interferograms a) 20150305-20150824 (linear), b) 20150418-20150601 (ERA5), c) 20150225-20150430 (NARR), and d) 20140124-20150209 (GACOS). The correction methods in brackets indicate the correction method that appears to be performing the poorest for each example. The legend shown in (a) is the same for each panel in the figure.

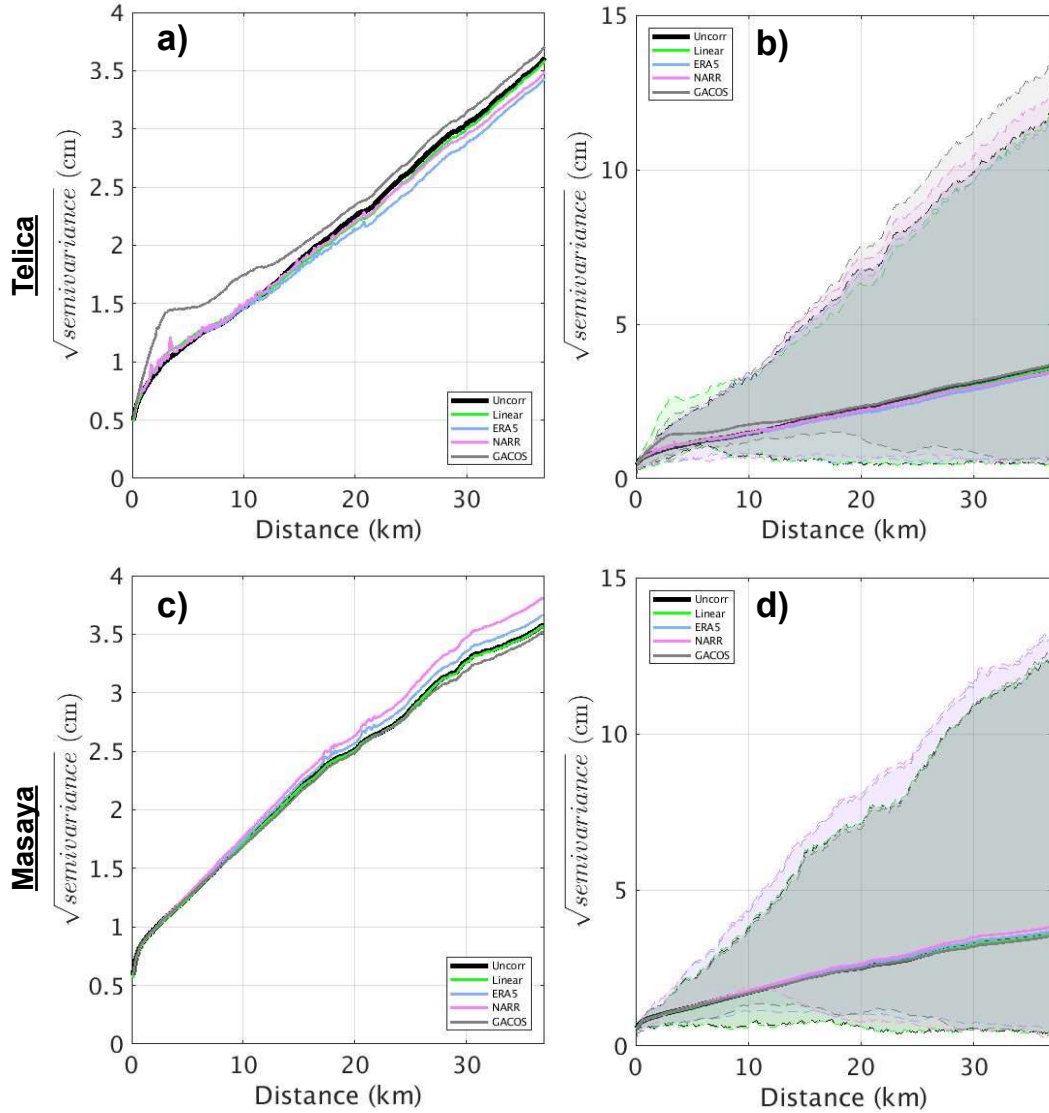


**Figure S7.** Averaged semivariogram plots for Telica and Masaya. These plots are similar to that of Figure S3, except here the lines indicate the averaged semivariance of all interferograms for each uncorrected and corrected InSAR dataset (a,c). Panels (b) and (d) include the averaged semivariance from panels (a) and (c), respectively, with the addition of shaded envelopes indicating the maximum and minimum semivariograms for the uncorrected and corrected datasets. Please note the y-axis scale for panels (a,c) are different from those shown in panels (b,d).

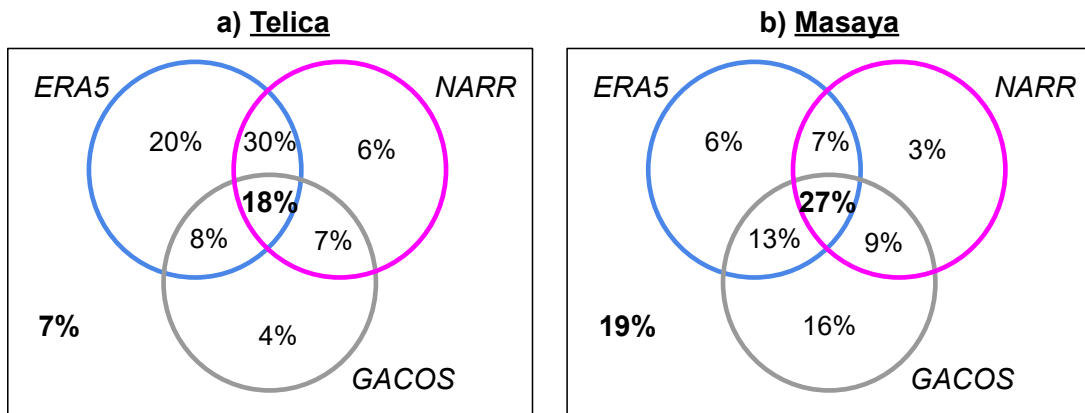


**Figure S8.** Venn diagrams displaying the results from visual assessment of the full scene phase-elevation plots for the GWM datasets only at a) Telica, and b) Masaya. Within the circles, each number represents the percentage of interferograms for which there was good agreement (similar spread in LOS phase and trend of the total phase delay map phase-elevation plot with the uncorrected interferogram phase-elevation plot). The numbers outside the circles represents the percentage of interferograms for which there was poor agreement (poor spread in LOS phase and/or opposite trend of the total phase delay map phase-elevation plot with the uncorrected interferogram phase-elevation plot).

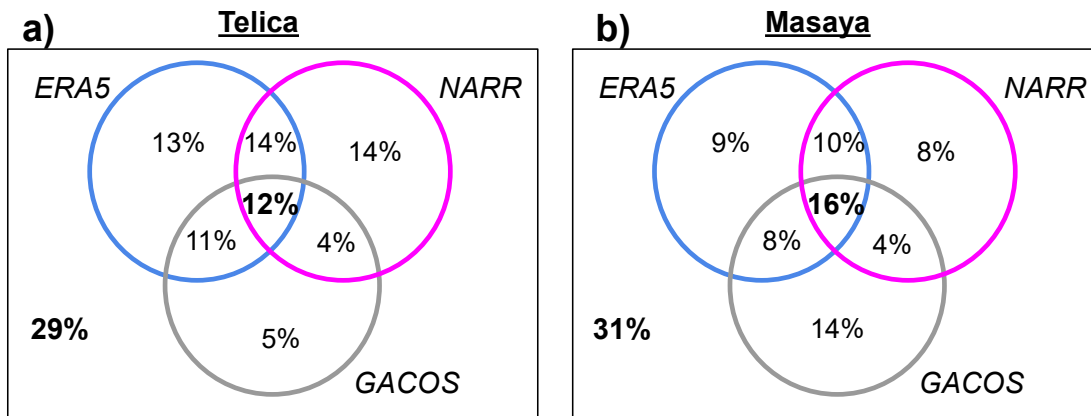


**Figure S9.** Venn diagrams displaying the variance reduction results for the GWM datasets only at a) Telica, and b) Masaya. Within the circles, each number represents the percentage of interferograms for which the GWM reduced the variance in the corrected interferogram. The numbers outside the circles represents the percentage of interferograms for which all GWMs demonstrated an increase in the variance for a single interferogram. The converse of these Venn diagrams (variance increase) are given in Figure 11.

#### Supplementary Material References

1. Lohman, R.B.; Simons, M. Some Thoughts on the Use of InSAR Data to Constrain Models of Surface Deformation: Noise Structure and Data Downsampling. *Geochem. Geophys. Geosyst.* **2005**, *6*. doi:10.1029/2004GC000841.
2. Knospe, S.H.-G.; Jónsson, S. Covariance Estimation for DInSAR Surface Deformation Measurements in the Presence of Anisotropic Atmospheric Noise. *IEEE Trans. Geosci. Remote Sens.* **2010**, *48*, 2057–2065. doi:10.1109/TGRS.2009.2033937.

3. Refice, A.; Belmonte, A.; Bovenga, F.; Pasquariello, G. On the Use of Anisotropic Covariance Models in Estimating Atmospheric DInSAR Contributions. *IEEE Geosci. Remote Sens. Lett.* **2011**, *8*, 341–345. doi:10.1109/LGRS.2010.2073440.
4. Jolivet, R.; Lasserre, C.; Doin, M.P.; Guillaso, S.; Peltzer, G.; Dailu, R.; Sun, J.; Shen, Z.K.; Xu, X. Shallow Creep on the Haiyuan Fault (Gansu, China) Revealed by SAR Interferometry. *J. Geophys. Res.* **2012**, *117*. doi:10.1029/2011JB008732.
5. Murray, K.D.; Bekaert, D.P.S.; Lohman, R.B. Tropospheric Corrections for InSAR: Statistical Assessments and Applications to the Central United States and Mexico. *Remote Sens. Environ.* **2019**, *232*. doi:10.1016/j.rse.2019.111326.
6. Matheron, G. Principles of Geostatistics. *Econ. Geol.* **1963**, *58*, 1246–1266. doi:10.2113/gsecongeo.58.8.1246.
7. Cressie, N.A.C. *Statistics for Spatial Data*, Revised ed.; John Wiley & Sons, Inc.: New York, NY, USA, 1993.
8. Trauth, M.H. Spatial Data. In *MATLAB Recipes for Earth Sciences*; Trauth, M.H., Ed.; Springer: Berlin/Heidelberg, Germany, 2015; pp. 249–314. doi:10.1007/978-3-662-46244-7\_7.
9. Wackernagel, H. Variogram Cloud. In *Multivariate Geostatistics: An Introduction with Applications*; Springer: Berlin/Heidelberg, Germany, 1995; pp. 30–34.
10. Bagnardi, M.; Hooper, A. Inversion of Surface Deformation Data for Rapid Estimates of Source Parameters and Uncertainties: A Bayesian Approach. *Geochem. Geophys. Geosyst.* **2018**, *19*, 2194–2211. doi:10.1029/2018GC007585.
11. Doin, M.-P.; Lasserre, C.; Peltzer, G.; Cavalié, O.; Doubre, C. Corrections of Stratified Tropospheric Delays in SAR Interferometry: Validation with Global Atmospheric Models. *J. Appl. Geophys.* **2009**, *69*, 35–50.
12. Jolivet, R.; Grandin, R.; Lasserre, C.; Doin, M.-P.; Peltzer, G. Systematic InSAR Tropospheric Phase Delay Corrections from Global Meteorological Reanalysis Data. *Geophys. Res. Lett.* **2011**, *38*. doi:10.1029/2011GL048757.
13. Jolivet, R.; Agram, P.S.; Lin, N.Y.; Simons, M.; Doin, M.-P.; Peltzer, G.; Li, Z. Improving InSAR Geodesy Using Global Atmospheric Models. *J. Geophys. Res. Solid Earth* **2014**, *119*, 2324–2341. doi:10.1002/2013JB010588.Received.
14. Bekaert, D.P.S.; Walters, R.J.; Wright, T.J.; Hooper, A.J.; Parker, D.J. Statistical Comparison of InSAR Tropospheric Correction Techniques. *Remote Sens. Environ.* **2015**, *170*, 40–47.
15. Parker, A.L.; Biggs, J.; Walters, R.J.; Ebmeier, S.K.; Wright, T.J.; Teanby, N.A.; Lu, Z. Systematic Assessment of Atmospheric Uncertainties for InSAR Data at Volcanic Arcs Using Large-Scale Atmospheric Models: Application to the Cascade Volcanoes, United States. *Remote Sens. Environ.* **2015**, *170*, 102–114. doi:10.1016/j.rse.2015.09.003.
16. Ebmeier, S.K.; Andrews, B.J.; Araya, M.C.; Arnold, D.W.D.; Biggs, J.; Cooper, C.; Cottrell, E.; Furtney, M.; Hickey, J.; Jay, J.; et al. Synthesis of Global Satellite Observations of Magmatic and Volcanic Deformation: Implications for Volcano Monitoring & the Lateral Extent of Magmatic Domains. *J. Appl. Volcanol.* **2018**, *7*, 26. doi:10.1186/s13617-018-0071-3.
17. Lin, Y.N.N.; Simons, M.; Hetland, E.A.; Muse, P.; DiCaprio, C. A Multiscale Approach to Estimating Topographically Correlated Propagation Delays in Radar Interferograms. *Geochem. Geophys. Geosyst.* **2010**, *11*. doi:10.1029/2010GC003228.
18. Emardson, T.R.; Simons, M.; Webb, F.H. Neutral Atmospheric Delay in Interferometric Synthetic Aperture Radar Applications: Statistical Description and Mitigation. *J. Geophys. Res.* **2003**, *108*. doi:10.1029/2002jb001781.
19. Wessel, P.; Smith, W.H.F. New, Improved Version of the Generic Mapping Tools Released. *EOS Trans. Am. Geophys. Union* **1998**, *79*, 579.



© 2020 by the authors. Submitted for possible open access publication under the terms and conditions of the Creative Commons Attribution (CC BY) license (<http://creativecommons.org/licenses/by/4.0/>).